THE ASTROPHYSICAL JOURNAL, 369:179–190, 1991 March 1

DYNAMIC EFFECTS ON CYCLOTRON SCATTERING IN PULSAR ACCRETION COLUMNS

J. J. BRAINERD[1]
NASA/Marshall Space Flight Center, ES 65, Huntsville, AL 35812
AND
P. MÉSZÁROS
525 Davey Lab, Department of Astronomy and Astrophysics, Penn State University, University Park, PA 16802
Received 1990 January 29; accepted 1990 August 22

ABSTRACT

The bulk infall motion of an X-ray pulsar accretion column alters the spectrum and the directionality of the primary radiation produced at the base of the polar cap. We examine this effect in the regime where the accretion column is optically thin to Thomson scattering and optically thick to resonant Compton scattering. Photons propagate freely through the column until the photon frequency equals the local cyclotron frequency, at which point the radiation is scattered, much of it back toward the star. The radiation pressure in this regime is insufficient to stop the infall. Some of the scattered radiation heats the stellar surface around the base of the column, which adds a softer component to the spectrum. The partial blocking by the accretion column of X-rays from the surface produces a fan beam emission pattern. X-rays above the surface cyclotron frequency freely escape and are characterized by a pencil beam. Gravitational light bending, which is one of several general relativistic effects present in this problem, produces a pencil beam pattern of column-scattered radiation in the antipodal direction. The interaction of radiation with the accretion column produces a cyclotron feature that is strongly angle-dependent.

Subject headings: pulsars — radiative transfer — stars: accretion — X-rays: sources

1. INTRODUCTION

The periodic variability of X-ray pulsar radiation demands angle-dependent emission from the magnetized accretion column. Using magnetic Compton cross sections, various authors have calculated cyclotron and continuum spectra from both homogeneous and multicomponent atmospheres with slab, cylinder, and cone shaped geometries (Yahel 1979; Nagel 1981; Pravdo & Bussard 1981; Langer & Rappaport 1982; Harding et al. 1984; Mészáros & Nagel 1985a, b; Wang, Wasserman, & Salpeter 1988, 1989; Mészáros & Riffert 1988). In each of these calculations, the atmosphere ends abruptly at a boundary with a vacuum. Ventura et al. (1985) and Soffel et al. (1985) model the effect of mass motion on the emergent spectrum in both the optically thin and thick regimes. Rebetzky et al. (1989), Kraus et al. (1989), and Maile et al. (1989) discuss the interaction of radiation with the accretion column for Thomson optical depths greater than unity, with particular emphasis on the redshift of the cyclotron resonance and the heating of the stellar surface near the accretion spot. Several authors examine phenomenological models for reprocessing by multicomponent systems: Basko & Sunyaev (1976) and McCray & Lamb (1976) consider the effect of reprocessing by an Alfvén shell; White & Holt (1982) and White & Stella (1987) consider reprocessing by an accretion disk; and Trümper et al. (1986) and Kahabka (1987) consider reprocessing by both an accretion disk and the stellar surface. These authors neglect the magnetic field and ignore dynamical effects.

We present in this paper a resonant scattering model for photon reprocessing in the accretion column. In this model, the accretion column is optically thin to Thomson scattering and optically thick to resonant scattering at the cyclotron frequency; this limits the model to accretion rates between $\approx 10^{34}$ ergs s^{-1} and $\approx 10^{37}$ ergs s^{-1}. Radiation from the neutron star surface propagates freely through the accretion column until the photon energy equals the local cyclotron frequency in the frame of the accretion stream. The radiation scatters at this point and propagates either to the observer or to the stellar surface. The emission from the stellar surface is coupled to the absorption of column scattered light. Outside of the accretion cap, the surface emits blackbody radiation at a rate that balances the absorption of radiation. The spectrum from the accretion cap is set to a model spectrum and is unaffected by the column radiation. This analysis uses the Schwarzschild metric in calculating photon orbital paths, photon redshifts, photon intensities, and the magnetic dipole field.

We investigate the angle-dependent spectra produced by this model and ascertain the relative importance of radiation from the accretion cap to that from the heated stellar surface and the accretion column. Shadowing of surface radiation by the accretion column and gravitational focusing of column radiation largely determine the broad range of angular behavior seen at different photon energies. The accretion column's motion transfers a fraction of the accretion luminosity to the column-scattered photons; the accretion column velocity is therefore less than the free-fall velocity. We show that this velocity decrease is negligible. Most of the soft X-rays are produced by the stellar surface outside the polar cap. Decreasing the column velocity decreases significantly the heating of the stellar surface, which decreases the soft X-ray production rate. Variation of the stellar compactness manifests this effect, as does setting the accretion velocity to zero.

The physics of this model is discussed in § 2. We discuss the details of our calculations in § 3 and in Appendices A and B. In § 4, we discuss our results, giving the temperature structure of the heated stellar surface and the spectrum from all components of our model. In § 5, we discuss the implications of our results for the observations and for subsequent theoretical investigations.

[1] Also Pennsylvania State University and University of Chicago.

2. PHYSICS OF THE BASIC MODEL

2.1. *Scattering and the Accretion Rate*

The Compton scattering cross section has a resonance at the cyclotron frequency. The existence of such a feature implies the existence of a regime for which the accretion column is optically thin to Thomson scattering and optically thick to resonant scattering. This occurs over a limited range of accretion rates. Below we define two accretion luminosities, L_l and L_u ($L_l < L_u$), that define this regime and the range of luminosities for which our conclusions are valid.

In the nonrelativistic limit, the total scattering cross section for an electron left in the ground state is (Herold 1979)

$$\sigma = \frac{\sigma_T}{2}\left\{\sin^2\theta + \frac{1}{2}(1+\cos^2\theta)\left[\frac{\omega^2}{(\omega+\omega_c)^2} + \frac{\omega^2}{(\omega-\omega_c)^2}\right]\right\}, \quad (1)$$

where σ_T is the Thomson cross section, ω is the angular photon frequency, $\omega_c = eB/m_e c$ is the local cyclotron frequency, B is the magnetic field strength, and θ is the propagation angle relative to the magnetic field. Ignoring the continuum part of the cross section, one can write the resonant part as

$$\sigma_R = \frac{\sigma_T}{4}\frac{(1+\cos^2\theta)\omega^2}{(\omega-\omega_c)^2 + \Gamma^2/4}, \quad (2)$$

where Γ, which is much less than ω_c, is the decay rate of the first Landau level. In the nonrelativistic limit one finds that $\Gamma = 4\alpha\epsilon_c\omega_c/3$, where $\epsilon_c = \hbar\omega_c/m_e c^2$.

The extreme narrowness of the cylotron resonance allows us to simplify the calculation of the optical depth along the magnetic axis by setting to constants all terms but the resonant term in equation (2). In these constant terms, and in the definition for electron density and radial position, all occurrences of ω_c are set to ω. Setting $\theta = 0$ in equation (2) and integrating over radius gives the resonant optical depth as

$$\tau_R = \frac{\sigma_T n_e}{2}\int_{R_0}^{\infty}\frac{\omega^2}{(\omega-\omega_c)^2+\Gamma^2/4}\,dR = \frac{\omega\sigma_T n_e R}{3\Gamma}\int_{-\infty}^{\infty}\frac{1}{1+x^2}\,dx = \frac{\pi\omega\sigma_T n_e R}{3\Gamma}, \quad (3)$$

where the integral over radius is replaced by an integral over cyclotron frequency. The dipole behavior of the magnetic field introduces a factor of 1/3. The nonrelativistic limit for Γ gives

$$\tau_R = \frac{\pi\sigma_T n_e R}{4\alpha\epsilon} = 1.1\times 10^3\sigma_T n_e R, \quad (4)$$

where we have set $\epsilon = 0.1$ on the far right.

We write the accretion luminosity for purely ionized hydrogen in the Newtonian limit as $L/f = 2\pi(R_S/R_0)^{3/2}R_0^2 m_p c^3 n_0$, where f is the fraction of the neutron star surface experiencing accretion, R_0 is the stellar radius, n_0 is the electron number density at the stellar surface, and $R_S = 2GM/c^2$ is the Schwarzschild radius. Setting $\tau_R > 1$ gives a lower limit on the accretion luminosity of

$$\frac{L_l}{f} = \frac{8\alpha m_p c^3 R_0\epsilon_c}{\sigma_T}\left(\frac{R_S}{R_0}\right)^{3/2} = 4.0\times 10^{36}\epsilon_c R_6\left(\frac{R_S}{R_0}\right)^{3/2}\ \text{ergs s}^{-1}, \quad (5)$$

where R_6 is the stellar radius in units of 10^6 cm. For a cyclotron frequency of $\epsilon_c = 0.1$, the lower luminosity limits are $L_l/f = 3.5\times 10^{34}R_6$ ergs s^{-1} for $R_0 = 5R_S$ and $L_l/f = 1.0\times 10^{35}R_6$ ergs s^{-1} for $R_0 = 2.5R_S$. Note that the optical depth defined above increases inversely with ω. For a dipole field and an $r^{-1/2}$ velocity field, where r is the distance from the neutron star's center, the density is proportional to $\omega_c^{5/6}$, while the length scale is proportional to $\omega_c^{-1/3}$. The optical depth is therefore proportional to $\omega^{-1/2}$. Consequently, for luminosities below L_l, the accretion column can be optically thick at high altitude and optically thin at the stellar surface this should be important for $L_l > L > L_l/3$.

Our requirement of a Thomson optical depth less than unity places an upper limit on the luminosity. For a dipole magnetic field and an $r^{-1/2}$ velocity field, one finds $\tau_T = 2\sigma_T n_0 R_0/3$. This gives

$$\frac{L_u}{f} = \frac{3\pi R_0 m_p c^3}{\sigma_T}\left(\frac{R_S}{R_0}\right)^{3/2} = 6.4\times 10^{38}R_6\left(\frac{R_S}{R_0}\right)^{3/2}\ \text{ergs s}^{-1}. \quad (6)$$

For $R_0 = 5R_S$, one finds $L_u/f = 5.7\times 10^{37}R_6$ ergs s^{-1}, while for $R_0 = 2.5R_S$, one finds $L_u/f = 1.6\times 10^{38}R_6$ ergs s^{-1}.

2.2. *Column Geometry and Radiation Propagation*

We assume that the X-ray pulsar is a neutron star with axisymmetric accretion occurring onto either one or both magnetic poles. The magnetic field has a dipole structure that is consistent with the Schwarzschild metric. Gas flows to the surface along magnetic field lines. Throughout this paper we consider accretion over the whole surface inside the half-angle θ_A—in other words, the accretion column is filled. Other than this restriction, knowledge of the variation of the plasma density in the accretion stream is unimportant in the calculations that follow. The polar cap input spectrum, which is assumed uniform across the accretion cap, is calculated with a magnetic Feautrier transfer code (Mészáros & Nagel 1985a, b) that includes polarization-dependent magnetic cross sections, Comptonization, and full angle and frequency dependence. We use the angle-averaged results.

Photons from the star's surface propagate freely through the accretion column until the photon energy equals the local cyclotron frequency in the frame of the accreting gas. Since the local cyclotron frequency decreases with distance from the star, the X-rays that scatter in the column are those with frequency below the surface cyclotron frequency. In this model, photons above the cylotron frequency cannot scatter with the fundamental cyclotron resonance, and therefore escape to infinity—in a more advanced model, these photons may scatter with higher cyclotron resonances. The inward motion of the plasma lowers the critical frequency above which photons escape.

Within the plasma frame, a scattering photon's energy does not change, but in the local rest frame, it changes through a Lorentz boost. The optical depth at the cyclotron resonance keeps the photon from propagating beyond the scattering surface. The time scale for a photon to random walk through the scattering surface is longer than the advection time scale by a factor of the scattering optical depth. All photons that scatter therefore escape in the direction of higher field strength.

A portion of the column-scattered spectrum propagates away from the star to infinity; the remainder strikes and heats the stellar surface, producing a circular ring around the polar cap with a temperature determined by the blackbody cooling rate. This assumption is one of convenience, as the true reprocessed spectrum consists of both a blackbody component and a complex backscattered component. The fraction of the surface heated in this way depends strongly on the gravitational bending of light. The circumpolar ring contributes a soft X-ray component to the radiation produced by the stellar surface. The amount of surface radiation that escapes to infinity depends on the shadowing of the surface by the accretion column. The significance of shadowing depends on the energy of the photon, the direction of the photon velocity relative to the plasma velocity, and the distance of the source from the accretion column base.

Radiation propagating from the accretion column to infinity is strongly focused by gravitational bending at the limb of the star. As a consequence, the column radiation is strongest in the antipodal direction. Figure 1 demonstrates the importance of gravitational bending. The propagation angle (ζ) at infinity relative to the magnetic axis is plotted for photons emitted from the magnetic axis. The emission height above the neutron star is given as the log of the local magnetic field strength relative to the surface field strength. The lower curves show ζ for a local emission angle of $\psi = 90°$ relative to the magnetic field axis. The upper curves show ζ for photons grazing the limb of the neutron star (see eq. [A5] and the following comment). The four sets of curves correspond to stellar radii of $R_0/R_S = 10$ (*bottom*), 5, 2.5, and 2 (*top*); there is, of course, more light bending for smaller radii and lower emission heights.

2.3. *Radiation Pressure*

Radiation pressure slightly modifies the velocity of the infalling material from the free-fall velocity. The effect is small even though the cyclotron resonance in the scattering cross section gives a resonant Eddington limit that is smaller than L_u. We prove this assertion below with the understanding that it applies only to an accretion stream at the surface of a neutron star.

The size of the resonant cross section implies a resonant Eddington limit that is much smaller than the classical Eddington limit (Mitrofanov & Pavlov 1982). The resonant Eddington limit is dependent on the shape of the surface radiation spectrum. For a Wien spectrum with temperature T in units of $m_e c^2$, we find that at the neutron star surface,

$$\frac{L_R}{f} = \frac{64 m_p c^3 R_S \alpha T}{3\sigma_T} \left(\frac{T}{\epsilon_c}\right)^3 \exp\left(\frac{\epsilon_c}{T}\right), \qquad (7)$$

$$= 1.1 \times 10^{37} \epsilon_c R_6 \left(\frac{R_S}{R_0}\right) \text{ ergs s}^{-1}, \qquad (8)$$

where we have set $T = \epsilon_c$ to obtain the last expression. If the initial spectrum is proportional to $\epsilon^2 \exp(-\epsilon/T)$, then the resonant Eddington limit is $\epsilon/3T$ times equation (7). Setting $\epsilon_c = 0.1$ in equation (8), we find the upper limits on the resonant Eddington limit of $L_R/f = 2.1 \times 10^{35}$ ergs s^{-1} for $R_0 = 5R_S$ and $L_R/f = 4.2 \times 10^{35}$ ergs s^{-1} for $R_0 = 2.5R_S$. These values fall just above L_l, so radiation pressure is capable of decelerating the accretion column in this model. In general, the resonant Eddington limit is higher, because the peak of the spectrum of X-ray pulsars lies below the cyclotron resonance.

The nature of the line pressure in the present problem is significantly different from that encountered in stellar winds. First, the radiation interacting with the accretion column is created by accretion rather than by an independent source. Second, the line frequency is determined by the local magnetic field strength rather than by the velocity of the gas. Third, the Doppler shift from the high infall velocity produces anisotropic scattering in the stationary frame. A consequence of these last two facts is that the radiation is not trapped in the line, but is scattered back toward the star to regions of low optical depth. Approximately $1/2\gamma^2$ of the radiation scatters to higher optical depths. For the stellar radii used in this paper, this fraction is less than 0.4. Therefore, approximately 0.99 of the photons scatter 5 times or less before escaping.

The small number of scatterings experienced by a photon suggests that a single scattering model for the radiative pressure is accurate. Two other factors suggest that conservation of momentum flux in one dimension describes the effect of radiation pressure on the accretion velocity, regardless of the number of scatterings a photon experiences before escaping. First, the region of high cross section for a particular photon frequency extends over a small range of magnetic field strengths, over which the column cross section is nearly constant, so adiabatic heating of the photons is insignificant. The sum of the plasma momentum flux and the photon momentum flux is therefore conserved along a streamline. The momentum transferred from a photon to the plasma equals the difference of the photon's final and initial momenta, and in the limit of zero electron recoil, which gives the maximum amount of momentum transferred from a photon to the plasma, multiple scatterings can be ignored. Second, for a particular frequency, the photon number density decreases as the optical depth increases along a magnetic field line, so the momentum flux carried by the photons is a minimum upstream and a maximum downstream of the interaction region. The momentum flux carried by the plasma is therefore a minimum downstream of the interaction region. These two points suggest that we can estimate the effect of radiation pressure on the accretion column from conservation of momentum across the interaction region.

For $L_R < L < L_u$, the accretion stream has a time-independent velocity that is a fraction of the free-fall velocity. This velocity is dependent on the free-fall velocity and the fraction of photons from the surface that interact with the column, but it is not directly dependent on the accretion rate.

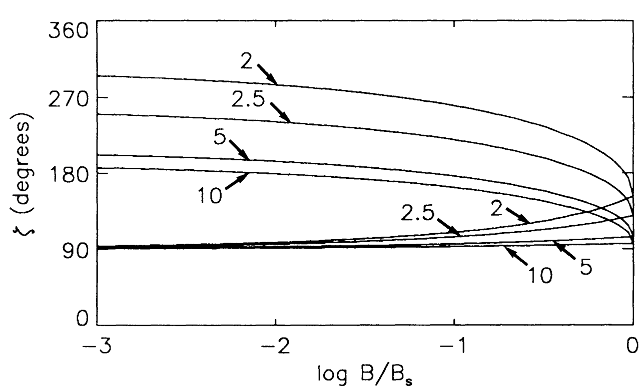

FIG. 1.—Gravitational bending of light. For radiation emitted from the magnetic axis, we plot the observed propagation angle ζ relative to the magnetic axis as a function of local magnetic field strength relative to the surface field strength. The lower curves are for an initial propagation angle of 90°, and the upper curves are for propagation paths that grazing the neutron star surface. The five different sets of curves correspond to five different stellar radii in units of the Schwarzschild radius.

To see that these statements are true, consider the momentum of the accretion stream and the maximum momentum that can be carried away by the radiation. The accretion stream transports momentum at the rate of $\dot{M}uc$ where $\dot{M}$ is the mass accretion rate and u is the dimensionless particle momentum. This rate is less than the free fall value of $\dot{M}u_0 c$, with the difference equal to the rate at which radiation removes momentum. The maximum blueshift a photon experiences on interacting with the accretion column is $\nu_f/\nu_i = (1+\beta)/(1-\beta)$, where ν_i and ν_f are the initial and final photon frequencies and β is the accretion velocity in units of c. The maximum amount of momentum carried away by each photon is then $[1 + (1+\beta)/(1-\beta)]h\nu_i/c = 2h\nu_i/c(1-\beta)$. The accretion rate gives a maximum photon luminosity of $\dot{M}(\gamma_0 - 1)c^2 = \dot{M}\gamma_0^2\beta_0^2 c^2/(\gamma_0 - 1)$. Therefore, the maximum rate at which momentum can be extracted from the accretion column is $2\dot{M}c\gamma_0^2\beta_0^2/(1+\gamma_0)(1-\beta)$. The actual momentum extracted rate is down by the factor $\chi < 1$, which describes geometric-, angle-, and frequency-dependent effects. Equating the momentum extraction rate to the difference between the momentum transport rate and the free-fall momentum transport rate, we find

$$u_0 = u + \frac{2\chi u_0^2}{(1+\gamma_0)}\gamma(\gamma + u) . \tag{9}$$

For $u = u_0$, the right side is larger than the left side. For $u = 0$, the right side equals $2\chi u_0^2/(1+\gamma_0)$, which is always smaller than the left side when $\chi < 1 + \gamma_0/2u_0$. The condition is satisfied for $\chi \leq 1$, when $u_0 \leq 4/3$ (when $\beta_0 \leq 4/5$). Because the right side increases montonically for $0 \leq \beta < 1$, this equation has a solution such that $\beta < \beta_0$. As examples of the solutions one finds, let $\beta_0 = 0.4$, which corresponds to a stellar radius of $R_0 = 6.25R_S$. Equation (9) then gives $\beta = 0.373$ and 0.293 for $\chi = 0.1$ and 0.5. When $\beta_0 = 0.6$, which corresponds to $R_0 = 2.78R_S$, we find $\beta = 0.540$ and 0.345 for $\chi = 0.1$ and 0.5.

3. DETAILS OF CALCULATION

3.1. *Coordinate Systems*

To simplify the calculation of light propagation, we transform from the coordinate system defined by the magnetic axis to the coordinate system defined by the initial and final photon positions. Both reference systems have their origins at the stellar center. In the field coordinate system, the $\hat{z}$ coordinate axis is the symmetry axis of the magnetic field, and the $\hat{x}$ axis lies in the plane defined by the observer and the $\hat{z}$ axis. The $\hat{x}$ coordinate of the observer's position is positive. The polar coordinates are (θ, ϕ).

In the propagation coordinate system, photon paths lie on planes of constant longitude. Two types of propagation occur—propagation between a point on the stellar surface and a point in the accretion column (Fig. 2), and propagation to the observer from a point either on the stellar surface or in the accretion column. In the first case, the $\hat{z}'$ axis passes through the point in the accretion column, while in the second case, $\hat{z}'$ passes through the observer. In both cases, the magnetic pole lies in the $\hat{x}'$-$\hat{z}'$ plane with $x' < 0$. The polar coordinates are (ζ, α).

One other coordinate system is relevant. It is the polar coordinate system defined by the proper angles measured in a stationary inertial frame. The first angle, which is defined as ψ in the accretion column and as ξ at the stellar surface (Fig. 2), is measured relative to the radial vector. The second angle, α, is the azimuthal angle as defined in the propagation coordinate system for a point in the accretion column.

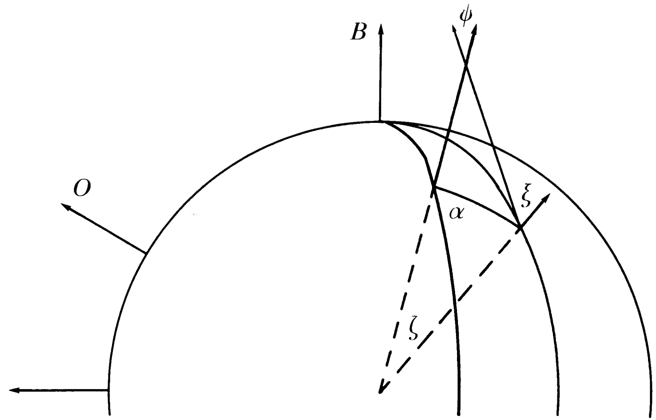

FIG. 2.—Coordinate systems. Several coordinate systems used in this paper are shown. The vector marked "O" is the direction of the observer, and the vector marked "B" is the magnetic axis. The propagation coordinates (ζ, α) between a point on the surface and a point in the accretion column are shown. The proper angle coordinate system is illustrated for the column (ψ) and for the surface (ξ).

3.2. *Magnetic Fields*

The magnetic dipole field for a Schwarzschild metric is given in Appendix B. Relativistic modifications to the field strength and field line shape are of order R_S/R_0. From equation (B3), one sees that to first order the magnetic field lines are given by

$$\frac{\sin\theta}{\sin\theta_0} = \left(\frac{r}{R_0}\right)^{1/2}\left[1 + \frac{3R_S}{8R_0}\left(1 - \frac{R_0}{r}\right)\right] . \tag{10}$$

The field lines spread more rapidly with coordinate distance in this case than in the Newtonian case.

From equation (B5), the field strength to first order is

$$B \propto r^{-3}\left[\left(1 + \frac{2R_S}{r}\right)\sin^2\theta + 4\left(1 + \frac{3R_S}{2r}\right)\cos^2\theta\right]^{1/2} . \tag{11}$$

The field strength decreases more rapidly with r in this case than in the Newtonian case. The physical consequences of these two effects is best illustrated by writing the equation for B in terms of angle θ along a magnetic field line. One finds

$$B \propto \sin^{-6}\theta\left[\left(1 + \frac{9R_S}{4R_0} - \frac{R_S\sin^2\theta_0}{4R_0\sin^2\theta}\right)\sin^2\theta + 4\left(1 + \frac{9R_S}{4R_0} - \frac{3R_S\sin^2\theta_0}{4R_0\sin^2\theta}\right)\cos^2\theta\right]^{1/2} . \tag{12}$$

As θ increases along a field line, the magnetic field decreases less rapidly than one expects for the Newtonian field. As a consequence, the scattering surface for a photon frequency of ν subtends a larger angle than in the Newtonian case.

3.3. *Redshift*

Two redshifts enter this problem. The first is from gravity, and the second is from the motion of the accreting gas. The gravitational redshift is $\epsilon_1\,(1 - R_S/R_1)^{1/2} = \epsilon_0(1 - R_S/R_0)^{1/2}$, where ϵ_0 is the photon energy at the stellar surface and ϵ_1 is the photon energy in the accretion column rest frame.

The velocity of the free-falling plasma in the local column coordinate system is $\boldsymbol{\beta} = -\beta(\hat{x}\cos\sigma + \hat{y}\sin\sigma)$, where

$\sigma < \pi/2$ is the angle between the radial unit vector and the magnetic field, as discussed in Appendix B (following eq. [B2]). In this paper, β is the locally measured free fall velocity in units of c. This is given by $\beta^2 = R_S/r$. The cyclotron frequency equals the photon frequency in the rest frame if

$$\epsilon_c = \epsilon_1 \gamma[1 + \beta(\cos \sigma \cos \psi + \sin \sigma \sin \psi \cos \alpha)] , \quad (13)$$

where $\gamma^2 = 1/(1 - \beta^2)$, and the photon is moving in the direction of ψ and α.

3.4. *Photon Propagation*

Propagation between the neutron star surface and a point in the accretion column is described by equation (A2), where R_1 is the radial component of the accretion column position. For integrals over the local column angle ψ that are limited to photon paths from the surface, we change the integration variable from ψ to ζ and multiply the integrand by the Jacobian in equation (A6). Propagation from the surface to an observer is given by equation (A2) with R_1 set to infinity and the constant Q defined at the surface through R_0 and ξ. These identifications also apply to equation (A6). Propagation from the accretion column to the observer is described by equation (A8), where R_1 is again the radial component of the column element. For $\psi < 90°$, the radial component of the photon path has a minimum of r_0, which is given by equation (A9).

3.5. *Local Photon Number*

In our calculations, we divide the accretion column into cells. The edges of these cells are defined by planes of longitude, magnetic field lines of constant θ_0, and surfaces with a constant ratio of local field strength to surface field strength as measured along lines of force. This last set of surfaces is defined through the variable $s = B(R_0, \theta_0)/B(r, \theta)$. The total number flux per unit area absorbed by the cell is found by integrating the number flux over ν, where the frequency is the resonant scattering frequency. This frequency is a function of s and the propagation angle of the photon. Taking the propagation angle, magnetic field direction, fluid velocity, and photon intensity as constant over the column cell, and taking surfaces of constant magnetic field strength for the scattering surfaces, the number of photons scattered per second is

$$\dot{N} = \int_{\nu_1(s+\delta s)}^{\nu_1(s)} \nu^{-1} I_\nu \hat{u}_p \cdot \hat{n}_B \, d\nu \approx I_\nu \hat{u}_p \cdot \hat{n}_B \nu_1^{-1} \int_{\nu_1(s+\delta s)}^{\nu_1(s)} d\nu , \quad (14)$$

where $\hat{u}$ is a photon's direction of propagation in the local coordinate system and $\hat{n}_B$ is the unit vector normal to the surface of constant magnetic field strength defined through equations (B6) and (B7) such that $\hat{n}_B \cdot \hat{r} > 0$. The integrand is set to zero when $\hat{u}_p \cdot \hat{n}_B < 0$. By definition, $\nu_B \propto s^{-1}$, and since the fluid velocity vector is assumed constant, $\nu_1 \propto s^{-1}$. The integral can therefore be written as

$$\nu^{-1} \int_{\nu_1(s+\delta s)}^{\nu_1(s)} d\nu = s^{-1} . \quad (15)$$

This gives

$$\dot{N} = I_\nu \hat{u}_p \cdot \hat{n}_B s^{-1} . \quad (16)$$

The total number of photons absorbed per second is then found by multiplying this by the cross section of the cell.

3.6. *Scattering Pattern*

We employ a very simple model for scattering at surfaces of constant magnetic field strength. The photons that scatter at a given field strength cannot propagate back to lower field strengths. We adopt a μ^2 scattering pattern in the rest frame, where $\mu = \hat{u}_p \cdot \hat{n}_B < 0$. In addition, we assume photons scatter isotropically within the plasma frame, producing an additional beaming factor of $\gamma^{-2}[1 + \beta(\cos \psi_B \cos \psi + \sin \psi_B \sin \psi \cos \alpha)]^{-2}$ in the rest frame. This expresses the effect of beaming on the total photon number. The total photon number flux scattered from the column element is then

$$\dot{N}_s = \dot{N} \mathcal{N}^{-1} \hat{u}_p \cdot \hat{n}_B \times [1 + \beta (\cos \sigma \cos \psi + \sin \sigma \sin \psi \cos \alpha)]^{-2} , \quad (17)$$

where $\mathcal{N}$ is a normalization defined so that the integral over solid angle for $\hat{u}_p \cdot \hat{n}_B < 0$ gives $\dot{N}$.

3.7. *Surface Heating*

A substantial fraction of the photons scattered by the accretion column are intercepted by the neutron star. We assume that all of the radiation striking the neutron star surface outside of the accretion cap is absorbed, and that the surface cools through blackbody emission. The reason for this assumption is that the scattering of X-rays in a neutron star's atmosphere is a complex process; its inclusion in this project would make the calculation and interpretation of spectra difficult. Our objective is to discern the effect of reprocessed surface emission on the observed spectrum, so a simple emission spectrum is desirable.

A considerable fraction of the energy striking the stellar surface is absorbed by the atmosphere through Compton scattering. An external flux of 50 keV photons striking the atmosphere of a nonmagnetic neutron star produces an emergent photon flux with 40% less energy (White, Lightman, & Zdziarski 1988). This lost energy reappears as blackbody radiation. The energy loss falls to approximately 15% of the input energy for 5 keV photons. Clearly blackbody emission is an important spectral component of the reprocessed surface emission, though modeling the reprocessed spectrum with a pure blackbody introduces some error in our model.

The heating of a unit surface area by scattering in a column element is calculated by multiplying the photon number per unit solid angle (eq. [17]) by the Jacobian in equation (A6), by $\cos \xi$ (eq. [A5]), and by the Doppler-shifted cyclotron energy—the gravitational redshift is canceled by the time dilation of the photon scattering rate. We find the surface temperature outside the accretion cap by equating the heating rate to the blackbody cooling rate. Because the blackbody photons also scatter in the accretion column, the temperature structure of the neutron star surface is found iteratively.

3.8. *Shadowing*

The accretion column shadows part of the neutron star surface from view. The strong angular dependence of the Doppler shift makes the shadowing strongly angle-dependent and difficult to calculate. We therefore approximate shadowing in the following manner. We calculate the angle between the observer and the magnetic axis and use the result in the Doppler shift formula. We then calculate the field strength at which a photon of a particular energy scatters. From this field strength, the altitude of the scattering surface at the column edge is calculated. If the photon travels inside the column at this altitude, we set the flux to zero; otherwise, we count the flux.

4. RESULTS

We present surface temperatures and spectra for systems with different values of the sine of the column opening half-angle ($\sin \theta_A$), the stellar radius R_0 (in Schwarzschild units), and the infall velocity in units of the speed of light $\beta = V_i/c$. We set the infall velocity to either the local free fall velocity or zero. The latter is used to investigate the effect of mass motion on the X-ray spectrum. Throughout this section we let the surface magnetic field strength be $B = 0.074 B_Q$, where $B_Q = 4.414 \times 10^{13}$ G. We express the flux as a distance scaled flux; that is, we let $L_\nu = D^2 F_\nu$, where D is the distance of the pulsar system. The units of this flux (ergs s^{-1} Hz^{-1} sr^{-1}) scale with the square of the physical radius and are defined for $R_0 = 10^6$ cm.

The effective temperature of the neutron star surface is shown in Figure 3 as a function of the cosine of the colatitude ($\cos \theta$) relative to the magnetic axis. The temperature is defined so that blackbody cooling equals heating from the absorption of column scattered radiation. The examples shown are for $R_0 = 5$ and $\sin \theta_A = 0.3$ (*left panel*), $R_0 = 2.5$ and $\sin \theta_A = 0.3$ (*center panel*), and $R_0 = 2.5$ and $\sin \theta_A = 0.1$ (*right panel*). In this figure and Figures 4–6, only one pole accretes. The input spectrum is the $\tau_T = 20$ moderate optical depth slab model of Mészáros and Nagel (1985b) averaged over angle and lowered in luminosity by a factor 10. The surface flux at the pole is identical in all three examples so that the luminosities are determined by the size of the star and the size of the accretion region. In our three examples, the total luminosities are $L/f = 1.3 \times 10^{38} R_6^2$ ergs s^{-1}, $L/f = 1.4 \times 10^{38} R_6^2$ ergs s^{-1}, and $L/f = 5 \times 10^{37} R_6^2$ ergs s^{-1}, all of which are near the upper limit defined in § 2. The dotted lines are for the static case ($\beta = 0$), while the solid lines are for the free fall case ($\beta = \beta_{ff}$). The heated area extends below the nonrelativistic horizon. As expected, higher thermalization temperatures are produced in the free-fall case, because the radiation is scattered downward with a larger blueshift. The effect of gravitational light bending is demonstrated by the temperature profile at large angles for the small radius star (*center panel*). Comparing the temperature profiles of the left and center panels, one sees that the small radius star, with its stronger gravitational light bending and higher free fall velocity, has a higher temperature profile than does the large radius star. The narrow column example (*right panel*) has a lower but flatter temperature profile outside of the accretion region than do the broad column examples. For a narrow column, the column length equals the column width close to the star, where the magnetic field is close to the surface value. Therefore, only photons in a narrow frequency band are scattered, and the heating of the surface is determined predominately by geometric effects. For broad columns, photons over a wide frequency band are scattered. Hard X-rays scatter at lower altitudes and heat regions close to the accretion cap; soft X-rays scatter high in the column and strike a large area of the surface far from the accretion cap. The temperature profile produced by a broad column is therefore determined by both geometry and the input spectrum, and decreases more rapidly with distance from the accretion cap than does the narrow column temperature profile.

In Figure 4, we show the input spectra from the polar cap (*long-dashed*) and the spectra emitted by the total surface (*solid* and *short dashed*). The radii and column opening angles are identical to those in Figure 3. These surface spectra are what one would see if the accretion column were empty; the true spectrum is much different, because much of the radiation is scattered as it passes through the accretion column to the observer. The effect of the infall velocity is shown in this figure; the infall velocity is $\beta = 0$ for the dotted lines and $\beta = \beta_{ff}$ for the solid lines. The three different sets of curves are for the following observer angles with respect to the magnetic axis: 28° (*top*), 57°.3 (*middle*), and 85°.9 (*bottom*). Notice that the surface spectra are significantly softer than the input spectra and exceed them in magnitude at low energies. This is true both for the static column ($\beta = 0$) and for the dynamic column ($\beta \neq 0$) but is significantly more pronounced for the latter. The spectra for the free falling column are a factor of 2 larger than those from the static column, which shows that, in soft X-ray production, the amount of kinetic energy extracted from the accretion column is as important as the fraction of photons scattered to the stellar surface. A narrow column, which scatters a small fraction of the radiation and scatters much more hard radiation than soft radiation, produces a less luminous and flatter soft spectrum than does a broad column.

The flux from the stellar surface is partially shadowed and reprocessed by the infalling material in the column. The shadowing of the free-fall surface spectra in Figure 4 is shown in Figure 5 under the approximation discussed at the end of § 3. One sees that the surface flux, which initially has a cyclotron

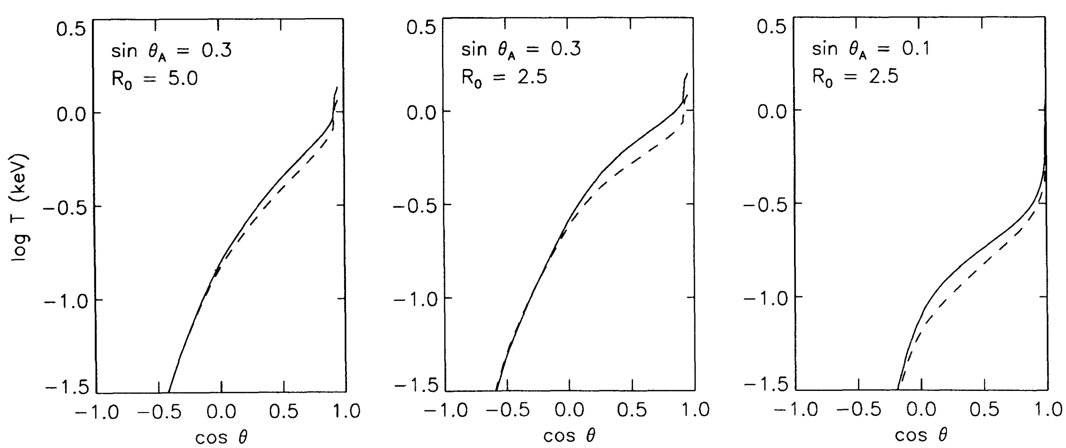

FIG. 3.—Neutron star surface temperature. The log of the neutron star surface temperature outside of the accretion cap is plotted in units of keV as a function of cosine of the colatitude. The solid curve is for a column in free fall, and the dashed curve is for a static column. The three different figures present results for different values of $\sin \theta_A$ and R_0.

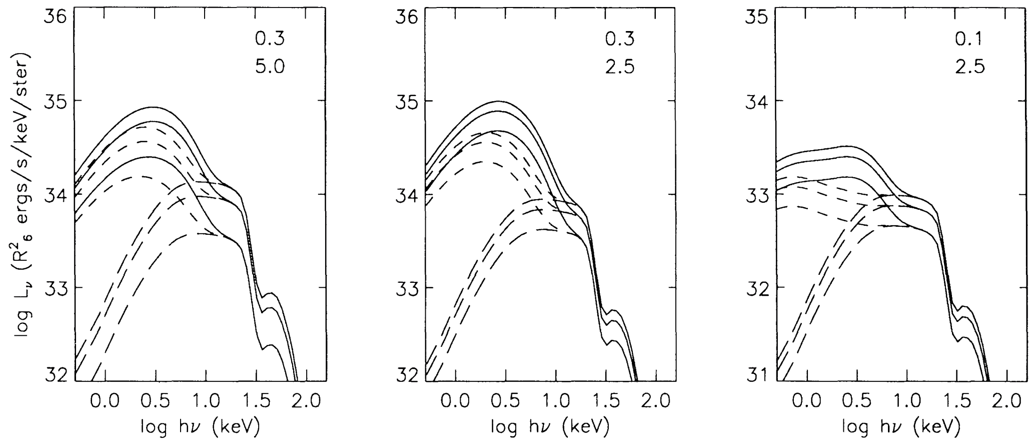

FIG. 4.—Unshadowed surface spectrum. The spectra obtained by adding the blackbody emission outside of the polar cap to the polar cap emission is plotted. The spectra are for a 10^6 cm radius star and scale as the radius squared. The surface temperatures outside of the polar cap are given in Fig. 3. The input polar cap spectra are plotted as long dashed lines, and the total surface spectra are plotted as solid lines for a free-falling accretion column and as short dashed lines for a static column. Three observer angles relative to the magnetic axis are used: 28°.6 (*uppermost curves*), 57°.3, and 85°.9 (*lowermost curves*). The three panels are for the same values of sin θ_A and R_0 as in the respective panels of Fig. 3.

"absorption" feature at the surface cyclotron resonance energy of 38 keV (cf. Fig. 4, *dashed lines*), acquires a second feature at a somewhat lower energy from cyclotron scattering in the column. This feature represents the cyclotron frequency in the frame of the infalling plasma at the surface of the neutron star. Its strong angular dependence arises from the angular dependence of the Doppler shift and is therefore much more apparent for stars of small radii, which have large free-fall velocities. The modification of the soft X-ray spectrum is strongest for small emission angles; for broad accretion columns, the small angle spectrum can drop below the large angle spectrum.

The escape of column scattered radiation to infinity produces the spectra in Figure 6. The spectra shown are for one-pole accretion only; for two polar caps, one adds spectra modulo 180°. These spectra correspond to the free-fall surface spectra of Figure 4. The various curves are for the observation angles of 85°.9 (*bottom*), 94°.1, 122°.7, and 151°.4 (*top*). The curve for 85°.9 is seen only for the large cap case because the photons scattered by the column leave in the direction of increasing field strength, so that $\theta \gtrsim 90° - \theta_A$. The larger angles exceed the Newtonian horizon because light bending allows one to "see" the accretion column over the horizon. Gravity focuses the radiation in the antipodal direction, producing a beam that becomes narrower and more intense as the stellar radius decreases. Hard X-rays, which scatter near the stellar surface, are strongly affected by gravitational light bending—the smaller the stellar radius, the larger the fraction of photons propagating to the stellar surface. As a consequence, the column-scattered spectra from stars with small radii peak at smaller frequencies than the spectra from stars with large radii.

The total observed spectrum which is the sum of the shadowed surface spectrum and the column scattered spectrum, is shown in Figure 7 for two-pole accretion at the free-fall velocity. The three panels correspond to the respective panels in Figures 3–6. The column-scattered component lessens the depth of the column produced cyclotron feature and adds complexity to the angular behavior of the soft X-rays. Column shadowing of soft X-rays is almost totally negated for a broad accretion column; this effect is much less dramatic for narrow columns.

The angular behavior of the flux for free fall accretion onto both magnetic poles is illustrated in Figure 8, which gives the flux for different photon energies as a function of the angle θ

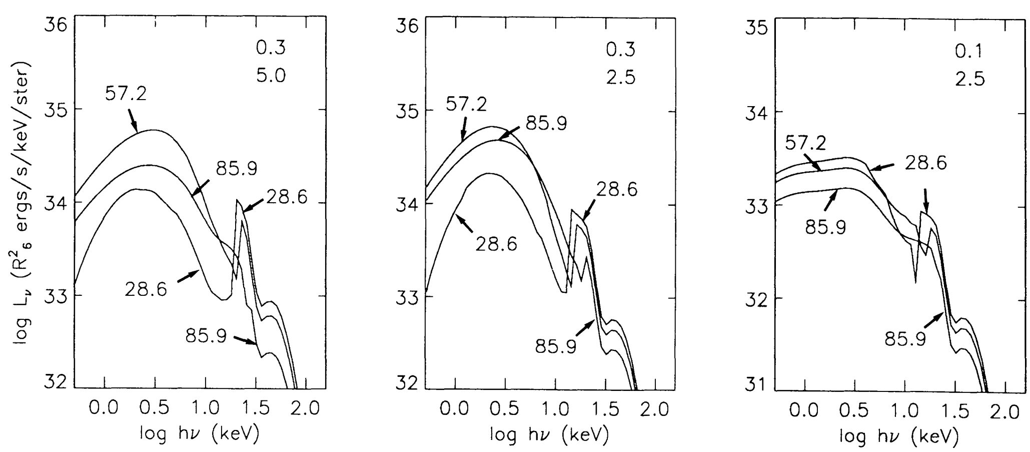

FIG. 5.—Shadowed surface spectrum. The column shadowed surface spectra for an accretion column in free fall is plotted for three different observer angles (in degrees). The values of sin θ_A and R_0 are as in the respective panels of Fig. 3.

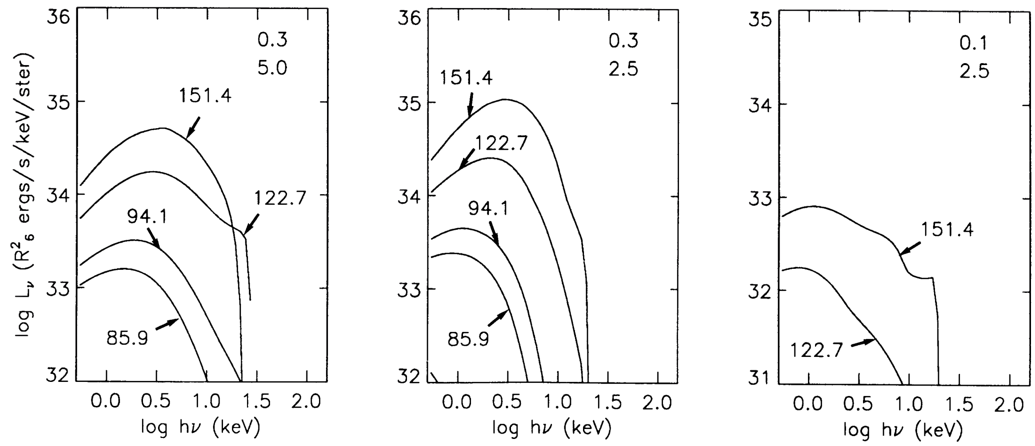

FIG. 6.—Beam-scattered spectrum. The spectra of radiation scattered by the accretion column and observed at infinity for different observer angles (in degrees). The values of sin θ_A and R_0 are as in the respective panels of Fig. 3.

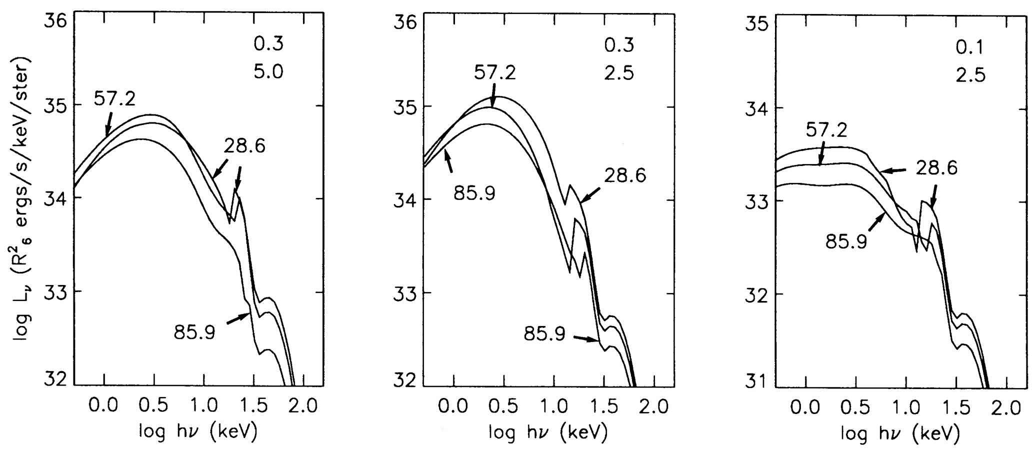

FIG. 7.—Total spectrum. These figures give the sum of the column-shadowed surface spectrum and the column scattered spectrum for a two-pole accretion model. Three different observer angles (in degrees) are used. The values of sin θ_A and R_0 are as in the respective panels of Fig. 3.

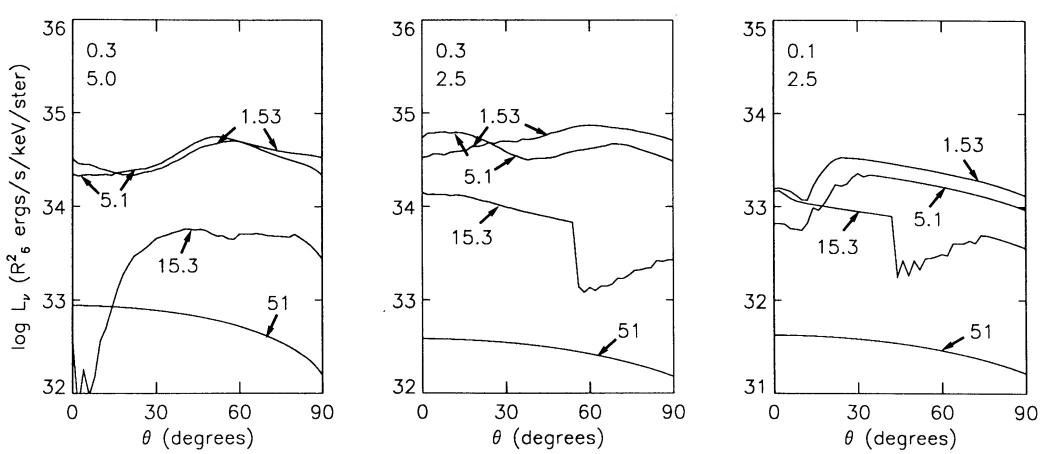

FIG. 8.—Angle-dependent fluxes. The total flux from a two-pole accretion model is plotted as a function of observer angle relative to the magnetic axis for the photon energies of 1.53, 5.11, 15.3, and 51.1 keV. The values of sin θ_A and R_0 are as in the respective panels of Fig. 3.

relative to the magnetic field as seen by a distant observer. The values of $\sin\theta_A$ and R_0 are identical to those in Figure 3. The photon energies are 51.1, 15.3, 5.11, and 1.53 keV. As seen in the center panel of Figure 8, the surface flux that is not significantly scattered (e.g., 51.1 keV) has a pencil-beam radiation pattern (largest at $\theta \sim 0°$) and shows the expected limb-darkening drop-off (approximately $\propto \cos\theta$). The next highest energy, 15.3 keV, shows this behavior at small angles, but as the angle increases through a critical angle, the cyclotron scattering opacity becomes large, and the surface flux drops rapidly. The discrete nature of our calculations do not permit us to fully resolve this drop. The source of this drop is the angle dependence of the Doppler-shifted cyclotron resonance. For small angles, the surface cyclotron line lies below 15.3 keV for $R = 2.5$. The cyclotron resonance is at 15.3 keV at the pole when the angle is $\cos\theta = R^{1/2}[\epsilon_c(1 - 1/R)/\epsilon - 1] = 0.775$, which is $\theta = 39°$. This is what is seen in the right panel of Figure 8 for a narrow column. In the wide-column case, the onset of the shadowing is delayed by approximately the width of the column, which is 17°. As the angle increases, the region of the accretion column shadowing the stellar surface moves to higher altitudes, and the occulted region progressively moves off of the stellar disk. This explains the gradual return to the unshadowed spectrum at large angles. In the left panel of Figure 8, the surface cyclotron frequency is always above 15.3 keV, so shadowing can occur at all emission angles. At lower energies, the central portion of the surface flux becomes absorbed. This produces an interpulse structure at low X-ray energies. One additional effect is the pulse maximum at $\theta = 0$ for 5.1 keV in the center panel. This is a consequence of strong gravitational focusing of column-scattered radiation.

5. DISCUSSION

The results of the previous section illustrate the physical role of a dynamic accretion column on the production of X-ray pulsar radiation. Scattering within the accretion column changes the spectrum and beaming pattern of X-rays through the heating and shadowing of the stellar surface and the scattering of radiation to the observer. The model used in this paper to study these effects assumes that only resonant scattering is important, which is a valid approximation for accretion rates between $10^{15} R_6 \beta f(\epsilon_c/0.1)$ g s^{-1} and $10^{18} R_6 \beta f$ g s^{-1}, where β is the surface infall velocity of the plasma.

The spectra from previously studied pure polar cap atmosphere models are modified below the cyclotron frequency in our composite model. In particular, the pure polar cap model produces a spectrum that turns over at low energies ($\lesssim$3–5 keV) to become a Planck spectrum with a characteristic temperature of 8–10 keV. This serious deficiency is not present in the column-scattering model; the thermalized circumpolar surface radiation comes from a much larger area than does the accretion cap radiation and therefore has a smaller effective temperature. The net effect of this (Fig. 4) is to boost the low-energy end of the total spectrum, so that a negative or flat power-law index can effectively represent it down to $\sim$2 keV (cf. the observational material; White, Swank, & Holt 1983).

It is important to note that the structure and shape of the cyclotron line, which in previous studies is dominated by the dense polar cap region (Mészáros & Nagel 1985a; Kii et al. 1986; Clark et al. 1989), is not significantly affected by the infalling column material. The cyclotron frequency in the accretion column, by virtue of the Doppler shift and the dipole decay law, assumes values smaller than the polar cap cylotron frequency. In the rest frame of the infalling matter, the spectrum from the static cap is blueshifted by the factor $(1 + v_{ff}\cos\theta/c)/(1 - v_{ff}^2/c^2)^{1/2}$, which is always greater than unity (there is a differential gravitational redshift factor that slightly offsets this). As a consequence, previous conclusions about the model interpretation of the line energy phase behavior (Mészáros and Nagel 1985a) that are based on pure static caps or cylinders are not affected by our present results.

The total radiation spectra show interesting features not previously encountered. At energies for which the spectrum is dominated by the input cap spectrum, i.e., $\omega \gtrsim 0.5\omega_c$, the spectrum has the same beaming as the static cap, which is pencil beamed for $R_0 \gtrsim 2.5$ (see Figs. 4 and 8). At lower energies, the transmitted cap flux becomes smaller along the polar axis and larger at large angles (Fig. 8), producing a fan beam. The portion of the down-scattered spectrum that is captured by the star is reradiated in a very broad hemispheric beam from the circumpolar area around the polar cap base. However, the portion of the reprocessed radiation that propagates at small angles to the magnetic field is scattered by the column and does not reach the observer. As a result, only the fan-beamed portion of the reprocessed spectrum is seen by an observer. Gravitational bending of the column scattered flux that escapes to infinity produces a pencil-beam radiation pattern in the antipodal direction (Fig. 8). The total radiation pattern calculated under the assumption of two symmetric polar caps is therefore a pencil beam at high energies, (51.1 keV in Fig. 8), an interpulse beam at lower energies (5.11 keV in Fig. 8), and a fan beam at even lower energies (1.53 keV in Fig. 8).

These results have interesting implications for the modeling of pulse shapes, since the present calculations indicate that, with our current understanding of what an accreting pulsar's emission region looks like, one should fit the data to a composite pencil-beam (hard) and fan-beam (soft) model. It is worth noting (e.g., Holt and McCray 1982; Nagase 1989) that in Her X-1 the very soft radiation ($\lesssim$1 keV) appears to be beamed 180° out of phase with respect to the radiation at energies $\gtrsim$2–5 keV. Presenting detailed models with these features would require a second paper that goes beyond the purposes of the present paper, which is to explore the qualitative properties and the physical basis of such second generation models.

From a comparison of Figure 4 (produced spectra) to Figure 5 (transmitted spectra) and Figure 7 (total spectra), one sees the effect of the infalling accretion column upon the input polar cap spectrum and the annular heated region around the cap, both of which are produced at rest. Our chosen cap spectrum has a single cyclotron line, while the thermalized annular region is blackbody. However, these flux components acquire a noticeable feature from cyclotron scattering in the infalling gas. The Doppler shift of the cylotron line in the accretion column places the column cyclotron feature at a lower frequency than the cap cyclotron feature. This secondary feature appears artificially sharp due to our approximation of a homogeneous column cross section (cf. previous section). In a more detailed column description, the differences in the velocity and density across the column will broaden this feature. If in a more realistic treatment the column cyclotron feature continues to look like a line, one must consider the possibility that the lines detected in Her X-1 and 4U 1538−52 are secondary features produced by the accretion column, and that the surface produced features at higher energies are in the sharp continuum drop-off. In such a case, the present estimates of the surface field are too small by a factor of $\sim$2.

On the other hand, variations of velocity and density across the accretion cap may smooth out the column cyclotron feature so that it no longer appears as a line, but rather as a shoulder with a high energy drop at $\omega \sim 0.5\omega_c$. We expect the shoulder to be similar in character to that seen in Figure 7. In comparison to the unscattered cap spectrum, the column would produce a spectrum with a more abrupt shoulder, which may give the appearance of a break in the power-law slope, such as that used to fit many accreting X-ray pulsar spectra (White, Swank, & Holt 1983). In such circumstances, the drop-off energy is not a thermal turnover but is rather a precursor signature of the surface cyclotron frequency. The shoulder occurs at an energy lower than the surface ω_c by $\Delta\omega \sim [v_{ff}(r_{sc})/c]\omega_c \sim R_0^{-1/2}\omega_c$. In reality, β is of order unity and cos $\theta < 1$, so this is a lower limit on $\Delta\omega$. For Her X-1, where $\omega_c \simeq 38$ keV (Voges et al. 1982), this gives $\omega \gtrsim 14$ for $R_0 = 2.5$. The observed drop-off energy is in fact a function of the pulse phase (Holt and McCray 1982), just as our shoulder drop-off energies are function of angle θ. Other factors such as polar cap opening angle and departures from azimuthal symmetry and cross section inhomogeneity should complicate things, but the above expression gives a lower estimate of the relative position of the shoulder and the line.

In summary, we have investigated an accreting pulsar model that incorporates several previously ignored physical elements and effects. It accounts for the reprocessing of polar cap radiation by the accretion column above it, as well as the reprocessing of column scattered radiation by the stellar surface surrounding the polar cap base. We find that these additions to the previously studied static atmosphere models enhance the softer portion of the spectrum at energies below about half the cyclotron energy and add a quasi-thermal low-energy component. We also find that the beaming characteristics at lower energies are significantly altered, so that the soft reprocessed spectrum is strongly out of phase with the original hard input spectrum.

This research has been supported in part through grants NASA NAGW-1522 and NSF AST 8815266 at Penn State University and NASA NAGW-830 and NAGW-1284 at the University of Chicago.

APPENDIX A

PHOTON PROPAGATION

The equation of motion for a longitudinal photon orbit in a Schwarzschild metric is

$$\left(\frac{dr}{d\zeta}\right)^2 = \frac{Q}{R_S^2} r^4 - \left(1 - \frac{R_S}{r}\right) r^2 , \tag{A1}$$

where Q is a constant and $R_S = 2GM/c^2$ is the Schwarzschild radius. We define $w = R_S/r$ and assume that $r > 3R_S/2$ in subsequent equations.

1. PROPAGATION FROM THE SURFACE

The angle traversed by a photon propagating from the neutron star surface R_0 to a radius R_1 above the surface is

$$\zeta = \int_{R_S/R_1}^{R_S/R_0} [Q - (1 - w)w^2]^{-1/2}\, dw . \tag{A2}$$

The constant Q is related to ψ, the propagation angle measured in the R_1 rest frame.

$$\cot \psi = \left.\frac{dl}{r\, d\zeta}\right|_{R_1} = \left(1 - \frac{R_S}{r}\right)^{-1/2} \left.\frac{dr}{r\, d\zeta}\right|_{R_1} = \left[\left(\frac{R_1}{R_S}\right)^2 \frac{Q}{1 - R_S/R_1} - 1\right]^{1/2} , \tag{A3}$$

which gives

$$Q = \left(\frac{R_S}{R_1}\right)^2 \left(1 - \frac{R_S}{R_1}\right) \csc^2 \psi . \tag{A4}$$

This constant is also related to ξ at R_0 in the same manner. The relation between ξ and ψ is therefore

$$\sin \xi = \frac{R_1}{R_0} \left(\frac{1 - R_S/R_0}{1 - R_S/R_1}\right)^{1/2} \sin \psi . \tag{A5}$$

The maximum values of ψ and ζ occur when the photon path grazes the limb of the neutron star, which occurs when $\sin \xi = 1$.

In this paper, we convert integrals over cos ψ into integrals over cos ζ when calculating the photon number flux passing through a given point in the accretion column. The Jacobian for this coordinate change is

$$J_{\psi,\zeta} = \left|\frac{d \cos \psi}{d \cos \zeta}\right| = \left|\frac{1}{\sin \zeta} \left(\frac{d\zeta}{d \cos \psi}\right)^{-1}\right| , \tag{A6}$$

where

$$\frac{d\zeta}{d \cos \psi} = -\frac{\cos \psi}{\sin^4 \psi} \left(\frac{R_S}{R_1}\right)^2 \left(1 - \frac{R_s}{R_1}\right) \int_{R_S/R_1}^{R_S/R_0} [Q - (1 - w)w^2]^{-3/2}\, dw . \tag{A7}$$

2. PROPAGATION FROM THE COLUMN TO AN OBSERVER

When a photon propagates from the accretion column to infinity, one must distinguish between $\sin\psi > 0$ and $\sin\psi < 0$; in the first case, the radius increases monotonically to infinity, while in the second case, the radius decreases to a minimum value of r_0 and then increases monotonically to infinity. The equations are

$$\zeta = \int_0^{R_S/R_1} [Q - (1-w)w^2]^{-1/2} dw + \begin{cases} 0\,, & \text{if } \sin\psi \geq 0\,, \\ 2\int_{R_S/R_1}^{R_S/r_0} [Q - (1-w)w^2]^{-1/2} dw\,, & \text{if } \sin\psi < 0\,, \end{cases} \tag{A8}$$

where

$$Q = \left(\frac{R_S}{R_1}\right)^2 \left(1 - \frac{R_S}{R_1}\right) \csc^2\psi = \left(\frac{R_S}{r_0}\right)^2 \left(1 - \frac{R_S}{r_0}\right). \tag{A9}$$

This last equation defines r_0. The maximum values of ψ and ζ are found by setting $r_0 = R_0$. A Jacobian relating ψ to ζ is not used for this aspect of the problem and is therefore not given.

APPENDIX B

MAGNETIC DIPOLE FIELD

The dipole magnetic field is modified by general relativistic effects. The field equations given below are derived from Wasserman and Shapiro (1983). As measured in the local rest frame, the two components of a dipole field are

$$B^{\hat\theta} = \frac{\mu \sin\theta}{r^3}\left(1 - \frac{R_S}{r}\right)^{1/2} b_\theta = \frac{\mu \sin\theta}{r^3}\left(1 - \frac{R_S}{r}\right)^{1/2} \sum_{i=0}^{\infty} \frac{3(i+1)}{i+3}\left(\frac{R_S}{r}\right)^i\,, \tag{B1}$$

$$B^{\hat r} = \frac{2\mu\cos\theta}{r^3} b_r = \frac{2\mu\cos\theta}{r^3} \sum_{i=0}^{\infty} \frac{3}{i+3}\left(\frac{R_S}{r}\right)^i\,, \tag{B2}$$

where μ is the dipole moment. The angle between the field and the radial vector in the local rest frame is $\tan\sigma = b_\theta(1 - R_S/r)^{1/2} \tan\theta/2b_r$. By definition, $0 \leq \sigma \leq \pi/2$. The equation for magnetic field lines is

$$\frac{\sin\theta}{\sin\theta_0} = \left(\frac{r}{R_0}\right)^{1/2} \exp\left[\frac{1}{2}\int_{R_0}^{r} f(r')r'^{-1}\,dr'\right], \tag{B3}$$

where θ_0 is the stellar surface value of θ and

$$f(r) = \frac{b_\theta}{b_r} - 1\,. \tag{B4}$$

The ratio of the field strength to the surface magnetic field strength is

$$\frac{B}{B_0} = \left(\frac{R_0}{r}\right)^3 \left(\frac{b_\theta^2(1 - R_S/r)\sin^2\theta + 4b_r^2\cos^2\theta}{b_{\theta 0}^2(1 - R_S/R_0)\sin^2\theta_0 + 4b_{r0}^2\cos^2\theta_0}\right)^{1/2}. \tag{B5}$$

The vector normal to surfaces of constant magnetic field strength as measured in the local rest frame is $\hat n_B = \hat r n_r + \hat\theta n_\theta$. The unit vectors are defined for Minkowski space and are oriented in the direction of decreasing field strength. The vector components are $n_r = c_r/(c_r^2 + c_\theta^2)^{1/2}$ and $n_\theta = c_\theta/(c_r^2 + c_\theta^2)^{1/2}$, where

$$c_r = \frac{3}{1 - R_S/r}\left\{\left[1 - \frac{R_S}{6r}\left(1 - \frac{R_S}{r}\right)b_\theta\right] b_\theta \sin^2\theta + 4b_r\cos^2\theta\right\}, \tag{B6}$$

$$c_\theta = [-b_\theta^2(1 - R_S/r) + 4b_r^2] \sin\theta\cos\theta\,. \tag{B7}$$

REFERENCES

Clark, G. W., et al. 1989, ApJ, in press
Basko, M. M., & Sunyaev, R. A. 1976, SovA, 20, 537
Harding, A. K., Mészáros, P., Kirk, J. G., & Galloway, D. 1984, ApJ, 278, 369
Herold, H. 1979, PhyRvD, 19, 2868
Holt, S. S., & McCray, D. 1982, ARAA, 20, 323
Kahabka, P. 1987, Ph.D. thesis, University of Munich (MPE Rep. 204)
Kii, T., Hayakawa, S., Nagase, F., Ikegami, T., & Kawawi, N. 1986, PASJ, 38, 751
Kraus, U., Herold, H., Maile, T., Nollert, H.-P., Rebetzky, A., Ruder, H., & Wolf, K. 1989, A&A, 223, 246
Langer, S. H., & Rappaport, S. 1982, ApJ, 257, 733
Maile, T., Bock, U., Herold, H., Rebetzky, A., Ruder, H., Ventura, J., & Wolf, K. 1989, A&A, 223, 251
McCray, R., & Lamb, F. K. 1976, Nature, 262, 356
Mészáros, P., & Nagel, W. 1985a, ApJ, 298, 147
———. 1985b, ApJ, 299, 138
Mészáros, P., & Riffert, H. 1988, ApJ, 327, 712
Mitrofanov, I. G., & Pavlov, G. G. 1982, MNRAS, 200, 1033
Nagase, F. 1989, PASJ, 41, 1
Nagel, W. 1981, ApJ, 251, 278

Pravdo, S. H., & Bussard, R. W. 1981, ApJ, 246, L115
Rebetzky, A., Bock, U., Herold, H., Kraus, U., Maile, T., Nollert, H.-P., Ruder, H., & Wolf, K. 1989, A&A, 225, 137
Soffel, M., Herold, H., Ruder, H., & Ventura, J. 1985, A&A, 144, 485
Trümper, J., Kahabka, P., Ogelman, H., Pietsch, W., & Voges, W. 1986, ApJ, 300, L63
Ventura, J., Soffel, M., Herold, H. & Ruder, H. 1985, A&A, 144, 479
Voges, W., Pietsch, W., Reppin, C., Trümper, J., Kendziorra, E., & Staubent, R. 1982, ApJ, 263, 803
Wang, J. C. L., Wasserman, I. M. & Salpeter, E. E. 1988, ApJS, 68, 735
———. 1989, ApJ, 338, 343
Wasserman, I. M., & Shapiro, L. S. 1983, ApJ, 265, 1036
White, N. E., & Holt, S. S. 1982, ApJ, 257, 318
White, N. E., & Stella, L. 1987, MNRAS, 231, 325
White, N. E., Swank, J., & Holt, S. S. 1983, ApJ, 270, 711
White, T. R., Lightman, A. P., & Zdziarski, A. A. 1988, ApJ, 331, 939
Yahel, R. 1979, ApJ, 229, L73